INSTITUTE OF PHYSICS PUBLISHING PHYSICS IN MEDICINE AND BIOLOGY

Phys. Med. Biol. **49** (2004) 4563–4578 PII: S0031-9155(04)79577-9

Pragmatic fully 3D image reconstruction for the MiCES mouse imaging PET scanner

Kisung Lee[1], Paul E Kinahan[1], Jeffrey A Fessler[2], Robert S Miyaoka[1], Marie Janes[1] and Tom K Lewellen[1]

[1] Department of Radiology, University of Washington, Seattle, WA 98195, USA
[2] Department of Electrical Engineering and Computer Science, University of Michigan, Ann Arbor, MI 48109, USA

E-mail: kinahan@u.washington.edu

Received 21 April 2004
Published 10 September 2004
Online at stacks.iop.org/PMB/49/4563
doi:10.1088/0031-9155/49/19/008

Abstract

We present a pragmatic approach to image reconstruction for data from the micro crystal elements system (MiCES) fully 3D mouse imaging positron emission tomography (PET) scanner under construction at the University of Washington. Our approach is modelled on fully 3D image reconstruction used in clinical PET scanners, which is based on Fourier rebinning (FORE) followed by 2D iterative image reconstruction using ordered-subsets expectation-maximization (OSEM). The use of iterative methods allows modelling of physical effects (e.g., statistical noise, detector blurring, attenuation, etc), while FORE accelerates the reconstruction process by reducing the fully 3D data to a stacked set of independent 2D sinograms. Previous investigations have indicated that non-stationary detector point-spread response effects, which are typically ignored for clinical imaging, significantly impact image quality for the MiCES scanner geometry. To model the effect of non-stationary detector blurring (DB) in the FORE+OSEM(DB) algorithm, we have added a factorized system matrix to the ASPIRE reconstruction library. Initial results indicate that the proposed approach produces an improvement in resolution without an undue increase in noise and without a significant increase in the computational burden. The impact on task performance, however, remains to be evaluated.

1. Introduction

Mouse imaging in positron emission tomography (PET) is increasing in significance due to its usefulness as a tool for biological research into disease processes and efficacy of therapeutic interventions. One of the main advantages is that small animal PET scanning allows

investigation of spatio-temporal changes of biological processes with serial and noninvasive measurements on the same animal (Chatziioannou 2002, Cherry 2004).

The micro crystal elements system (MiCES) is a fully 3D mouse imaging PET scanner (Miyaoka *et al* 2001) under construction at the University of Washington. This paper presents the initial results of a 'pragmatic' approach to image reconstruction for data from the MiCES scanner. Our method is modelled on the hybrid approach to fully 3D image reconstruction used in clinical PET scanners (Comtat *et al* 1998), which is based on Fourier rebinning (FORE) (Defrise *et al* 1997) followed by 2D iterative image reconstruction, such as ordered-subsets expectation-maximization (OSEM) (Hudson and Larkin 1994). In human scanners the dominant effect on image noise was determined to be attenuation, and so only this effect was included in the Poisson model used by OSEM as an attenuation weighting (AW). This led to the FORE+(AW)OSEM algorithm, which is now implemented in many clinical PET scanners for routine 3D clinical PET imaging (Comtat *et al* 1998). By using Fourier rebinning and only considering attenuation, that is, neglecting to model other physical effects in the data statistics, the computation time of the image reconstruction remains clinically feasible without significantly degrading image quality (Liu *et al* 2001).

The limiting factor in image quality for many PET studies is the high levels of statistical noise. This is potentially even more of an issue for imaging studies of mice, as only small volumes (typically 100 μl or less) of radio-labelled tracers can be injected due to the small blood volume of mice (typically on the order of 2 ml).

One method of reducing statistical noise is to increase the sensitivity of the scanner. This can be done by operating the scanner in fully 3D acquisition mode (Chatziioannou *et al* 1999). This acquisition mode increases the sensitivity by a factor of approximately five- to ten-fold, but increases the computational demands for data storage and image reconstruction.

An alternate method of reducing statistical noise in the reconstructed image is to use a model of the Poisson-distributed imaging statistics in the reconstruction algorithm. However, the resulting set of equations describing the forward problem becomes very large and nonlinear, and solving for the tracer distribution by direct inversion of the forward problem becomes intractable. In this case, the equations must be solved using iterative methods.

Several methods of image reconstruction for small animal PET scanners that combine fully 3D imaging and iterative reconstruction have been developed (e.g. Johnson *et al* 1997, Qi *et al* 1998, Selivanov *et al* 2000, Leahy and Qi 2000, Reader *et al* 2002, Frese *et al* 2003). Among these works, the studies by Qi *et al* (1998), Leahy and Qi (2000) proposed an accurate fully 3D method made tractable by using a factorization of the system matrix into independent matrices corresponding to approximations of sequential physical effects that occur in the data stream of a PET scanner.

In previous studies (Lee *et al* 2004) we have determined that for ^{18}F-labelled tracers the most significant physical effect for mice imaging is the non-stationary detector blurring (DB). This is due to the unknown depth of interaction of the individual annihilation photons in the detector system as illustrated in figure 1.

Anti-collinear photons from a positron–electron annihilation that are detected in time-coincidence form a line of response. Compton scatter and other processes lead to uncertainty in the true locations of the line of response endpoints in both the transverse and axial directions (for multi-ring scanners). As the line of response is moved to the edge of the field of view (FOV), however, the annihilation photons enter the detectors at a more oblique angle, thus passing through more material and broadening the PSF. In addition the probability of interaction decreases along the initial photon path through the scintillator, leading to an asymmetry in the PSF. Similar effects occur in the axial direction.

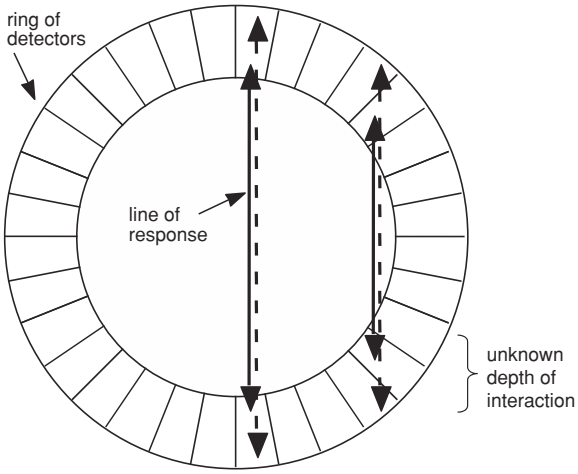

Figure 1. Illustration of physical effects leading to non-stationary detector response for PET scanners.

We therefore combined FORE+OSEM with a DB model using a factorized system matrix to the ASPIRE (Fessler 2001, 2002 and 2003) reconstruction library. A similar approach was studied by Liang (1994). We also included the first-order effect of FORE rebinning on sinogram variance. This approach (termed FORE+OSEM(DB)) trades off some accuracy in the reconstructed image relative to the gold standard methodology of Leahy and Qi (2000) in favour of reducing computation time. The use of the ASPIRE library, however, allows for potential utilization of more sophisticated algorithms with proved convergence, which OSEM does not have.

The proposed FORE+OSEM(DB) algorithm was used to reconstruct simulated data and measured data from a single-ring MiCES evaluation system (Miyaoka *et al* 2003) at the University of Washington. These results were also compared with FORE+FBP and FORE+OSEM. In the FORE+OSEM implementation attenuation weighting was not used due to the small amount of attenuation in a mouse scan. For both the simulated and measured data the PSF was two dimensional on the detector surface for each end of the line of response. In the image reconstruction, however, only the transverse effect was modelled. The simulation studies were used to test the basic efficacy of the approach where we have perfect knowledge of the detector blurring. For the measured data from the evaluation system we did not attempt to simulate the detector PSF, but rather used an estimate of the transverse PSF blurring derived from line source measurements.

2. Methods

2.1. Simulation studies

2.1.1. The MiCES scanner and a simplified model. The full MiCES machine will consist of four rings (12 cm diameter), with each ring comprising 18 position sensitive photomultiplier tube (PMT) detector module blocks (see figure 2(a)). The scanner utilizes a total of 72 PMTs (18 blocks $\times$ 4 rings), each coupled to a 22 $\times$ 22 array of 0.8 $\times$ 0.8 $\times$ 10 mm discrete mixed lutetium silicate (MLS) crystals. There is a 0.1 mm inter-crystal gap between adjacent crystals. In modelling the scanner for this study, the target detector modules were simplified into figure 2(b). In the simplified model, a ring was divided into 396 equally spaced discrete

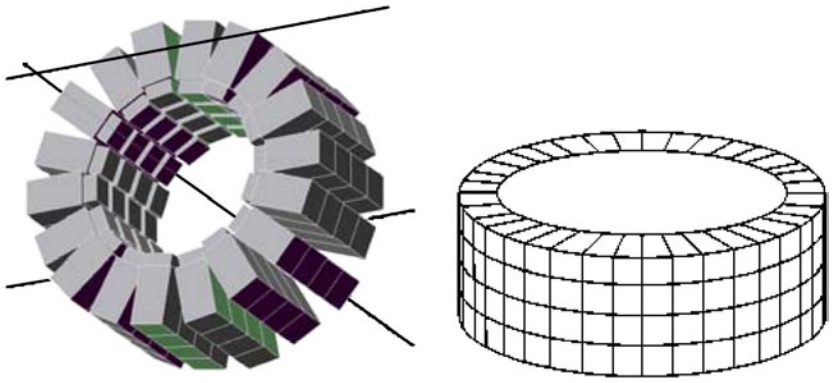

(a) (b)

Figure 2. (a) Detector module arrangement for the MiCES scanner, (b) simplified model used for the simulation studies.

crystals (22 crystals $\times$ 18 blocks) along the circumference of the ring. In the axial direction, four rings were split into 88 crystals (22 crystals $\times$ 4 blocks). Keeping the same detector ring diameter, the crystal cross-sections were 1×1 mm^2. No gap was considered between adjacent crystals and the length of the crystals was 10 mm. The model does not exactly replicate the anticipated geometry of the MiCES scanner, as the goal of the simulation is to evaluate the general efficacy of including at least the transverse component of the PSF detector blurring in the image reconstruction process.

2.1.2. Detector point-spread function generation. Spatially-varying detector point-spread functions (PSFs) in the projection (sinogram) domain were simulated using SimSET for the simplified model of MiCES described above. The simulation tracked annihilation photon interactions in the detectors, but did not consider the effects of optical photon transport from the scintillation sites (Mumcuoglu *et al* 1996, Lee *et al* 2004). By simulating collimated beams of annihilation photons at every radial position, detector PSFs were obtained for each transverse sinogram bin. These results were then used to model the detector blurring in the image reconstruction. We note that this PSF modelling does not account for blurring in the axial direction, or for non-stationary effects in the axial direction for oblique lines of response. Stationary and non-stationary axial blurring effects, however, were included in the simulations.

2.1.3. Reconstructed point sources. A point-source phantom that spans most of the volume of the FOV was generated to investigate the performance of the FORE+OSEM(DB) algorithm within the FOV. The sources were spheres 2 mm in diameter positioned 0, 12 and 24 mm from the transaxial centre, and 0, $\pm$10 and $\pm$20 mm from axial centre of the FOV. A water equivalent, cylindrical attenuation object was generated to cover the entire field of view. The test phantom is illustrated in figure 3. Fully 3D listmode data were generated for the test objects by SimSET including all annihilation photon transport effects. The listmode data were binned into oblique sinograms with a maximum ring difference of 44 (axial acceptance angle of 19°). The oblique sinograms were then rebinned into a stacked set of 2D sinograms using single-slice rebinning (SSRB) and FORE.

The system matrix was generated on the basis of parallel strip-integrals with a 0.3 mm strip width. Images were reconstructed with FORE+FBP, FORE+OSEM and FORE+OSEM(DB). In addition we also considered the SSRB, which is a very fast and compact method (Daube-Witherspoon and Muehllehner 1987). As shown by Matej *et al* (1998), however,

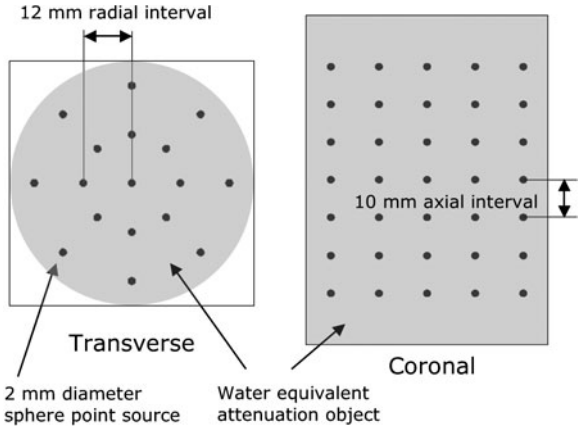

Figure 3. Test phantom used for simulation studies.

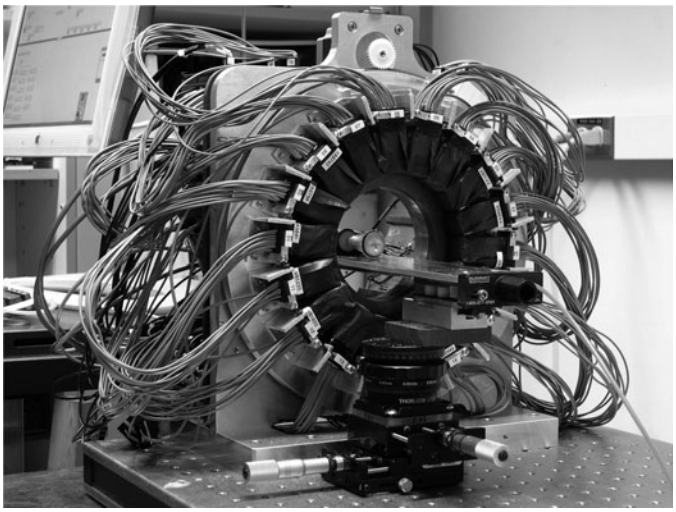

Figure 4. Single-ring MiCES evaluation system (QuickPET II).

the SSRB introduces severe distortions of data in both transverse and coronal planes while the FORE produces data with similar quality throughout the whole FOV area. As discussed in the results section, the SSRB was not explored further in this study. All OSEM images were reconstructed with four iterations of nine subsets. The detector blurring was incorporated following the factorized system matrix approach of Leahy and Qi (2000) where the non-stationary detector blurring is applied in the projection domain as a separate operation after the forward projection operation in each of the OSEM iterates.

2.2. Measured data from the MiCES evaluation system

The FORE+OSEM(DB) image reconstruction method was applied to measured data acquired from the single-ring MiCES evaluation system called QuickPET II (Miyaoka *et al* 2003) shown in figure 4. It has one ring (12.65 cm diameter) of 18 detector arrays, each coupled to a position sensitive PMT block. PMT and crystal specifications are the same as those described

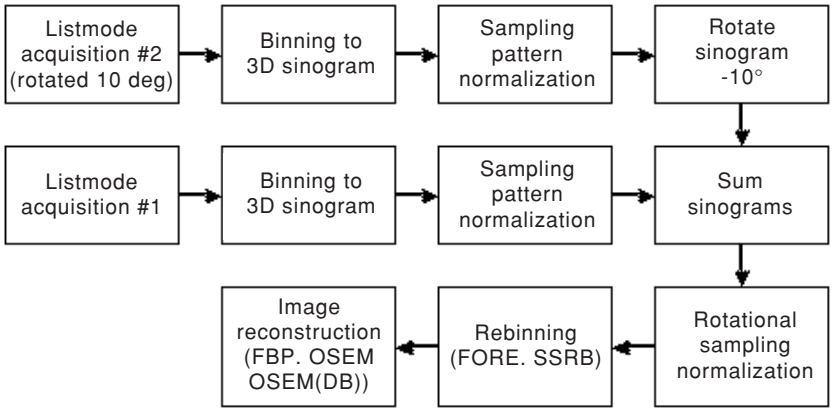

Figure 5. Data processing of measured listmode data for the QuickPET II scanner.

in section 2.1. The transverse FOV diameter is 5.76 cm, and the axial length of the FOV is 1.98 cm.

The full MiCES scanner with four rings will rotate continuously around its major axis for gap compensation. The current evaluation system, however, provides computer-controlled rotation of $\pm 10^{\circ}$.

2.2.1. Data processing. For the prototype evaluation, all coincident data are acquired in listmode format and then histogrammed into fully 3D sinograms for quantitative corrections and image reconstruction. A second listmode data set is acquired after rotating the detector ring 10° between the acquisitions. This is to measure those regions in the first sinogram that are unmeasured due to the gaps between adjacent detector modules. The data processing procedures for the current evaluation system, from collecting data through image reconstruction, are illustrated in figure 5.

The first procedure was to estimate the true detector positioning offsets before histogramming the data into sinograms. These offsets were estimated by comparing simulations and measurements of two axially oriented line sources (described below) located 0 and 14 mm radially from the centre of the field of view. The 18 detector blocks were considered as 9 opposed pairs of detectors. For each pair of detectors, noise-free sinograms were simulated with each of the two detectors in a 5×5 grid of transverse offsets in the x and y directions, thus resulting in 625 simulated sinograms for each pair of detectors. The grid points for the detector locations were separated by 0.225 mm, or $1/4$ of the centre-to-centre detector element spacing. The minimum root-mean-square error (RMSE) between the corresponding region of the measured sinogram and the nonzero regions of the simulated sinograms were computed, and the transverse offsets corresponding to the minimum RMSE were chosen as the locations of the detector block. This was repeated for each of the nine detector pairs. We note that these corrections do not account for the z-axis (scanner axis) offsets of the detector blocks or rotational offsets. Methods for these calibrations are currently under development. We also note, however, that the transverse offsets of the detector blocks are likely to be the most important positional offsets. The estimation of the detector block offsets was only performed once.

With the transverse detector offsets accounted for, both listmode data sets are binned into fully 3D sinograms with equi-spaced projection rays. In other words there is no detector arc-effect in the sinogram data from the detector ring curvature, unlike sinograms that directly

map detector pair combinations (Defrise and Kinahan 1998, p 17). This binning, however, introduces a systematic bias in the sinogram due to the variable number of detector pair combinations that contribute to each sinogram bin. This bias is easily estimated (and then corrected for) by generating a listmode data file with one coincident event per detector pair combination. The next phase would normally be to correct for variations in individual detector efficiencies. However, we have not yet implemented a robust procedure for implementing detector efficiencies, so no efficiency corrections were applied.

The second sinogram is then rotated (shifted in azimuthal coordinate) by 10° to match the orientation of the first sinogram, and then added to the first sinogram. This compensates for the missing data due to the detector gaps, but necessitates a second normalization to compensate for the varying additions to each sinogram bin. Other quantitative corrections for attenuation and scattered and random coincidences are currently not implemented due to limitations of the current experimental environment. The fully 3D sinograms are then rebinned into a stack of 2D sinograms, which are then reconstructed as described in section 2.1 with FBP, OSEM or OSEM(DB).

2.2.2. Detector blurring point-spread functions. A requirement for the proposed reconstruction approach is to estimate the spatially varying detector PSFs. Since collimated point source measurements are difficult to perform, we instead acquired line source data to estimate only the transverse detector blurring PSFs. The line sources were 0.3 mm inner diameter capillary tubes 6 cm in length. Two tubes were each filled with ∼16 μCi (592 kBq) of ^{18}F. The tubes were placed parallel to one another, and 14 mm apart on a thin, stiff board. The two capillary tubes were oriented axially and positioned at 0 mm (tube 1) and 14 mm (tube 2) radial distance from the FOV centre. A total of 600 000 coincident events (2000 counts s^{-1} × 5 min) were acquired. The tubes were stepped out radially in seven increments of 2 mm. This procedure was used to allow fitting parametric profiles to the tranverse profiles in the sinograms down to the tenth-maximum level. If we had simultaneously acquired 14 line sources separated by 2 mm, the tails of each profile would have overlapped. A total of 600 000 coincident events were collected for each acquisition. The detector ring was then rotated by 10° and the acquisitions were repeated.

The listmode data were binned into fully 3D sinograms, and processed as described above up to the point prior to FORE rebinning, resulting in seven fully 3D sinograms. Some signal averaging was found to be necessary to alleviate the noise in the profiles. This was done with SSRB rebinning with ±5 ring difference (±2°), and axial summing of the central 10 (out of 43) 2D sinograms. The 1D projection at azimuthal angle of zero (perpendicular to the line sources) was extracted from each averaged sinogram. Each profile contained two peaks that were separately fit to a parametric function as described next.

2.2.3. Parametrization of detector blurring PSF. After acquiring profiles from line source sinograms, the PSFs were fit with an asymmetrical Gaussian–Lorentzian curve to allow robust interpolation for all transverse sinogram bins according to

$$f(x) = \begin{cases} a\left(w\exp\left(-\dfrac{(x-\mu)^2}{2\sigma_1^2}\right) + (1-w)\left(1\Big/b_1\left(1+\left(\dfrac{x-\mu}{b_1}\right)^2\right)\right)\right), & |x| \leqslant |\mu| \\ a\left(w\exp\left(-\dfrac{(x-\mu)^2}{2\sigma_2^2}\right) + (1-w)\left(1\Big/b_2\left(1+\left(\dfrac{x-\mu}{b_2}\right)^2\right)\right)\right), & |x| > |\mu| \end{cases} \tag{1}$$

where w is a weight representing contribution of the Gaussian term, and μ is the estimated peak location of $f(x)$. The $(1-w)$ contribution of the Lorentzian curve allows for the presence of broad tails in the PSF. Since the PSFs are potentially asymmetric, the shape of the function was divided into two halves centred on the peak value of x ($x = \mu$), and fitted with different Gaussian (σ_1, σ_2) and Lorentzian (b_1, b_2) half-width parameters, i.e. σ_1, b_1 for the broader half towards the FOV centre, and σ_2, b_2 for the narrower half towards the FOV boundary. The curve-fitting results of equation (1) were then plotted as a function of transverse position $x = \mu$. Detector PSFs at intermediate transverse positions were then generated by estimation from linear fits to these parameters as a function of position.

2.2.4. Image reconstruction of line source measurements. The combined line source listmode acquisitions were histogrammed into fully 3D sinograms and rebinned into a stacked set of 2D sinograms by FORE rebinning with a maximum ring differences of ± 21 ($\pm 8.5^\circ$ acceptance angle). Images were reconstructed by FORE+FBP (with a ramp filter), FORE+OSEM and FORE+OSEM(DB) with detector blurring.

2.2.5. Reconstruction of mouse cardiac images. The measured detector blurring was incorporated into the system model as described above to reconstruct acquired mouse sinogram data.

A p53 heterozygote female mouse on an NIH background with chemically induced skin tumours was imaged with FDG. The mouse was injected with 240 μCi (8.88 MBq) of FDG via tail vein injection. Imaging began approximately 1 h post-injection. To reduce uptake in the background tissues, the mouse was kept under light anaesthesia (0.5–2.0% isoflurane) during radiopharmaceutical uptake. A five field of view scan was acquired over $\sim$90 min. A total of 21.3 million events were acquired during the study. Images were reconstructed with FORE+FBP (with a ramp filter), FORE+OSEM and FORE+OSEM(DB), and sections of the images through the left ventricle were evaluated.

3. Results

3.1. Simulation studies

3.1.1. Detector point-spread function generation. Figure 6 shows detector PSFs at the locations of 0, 12 and 24 mm radially off-centre from the field-of-view centre. As the source position approaches the FOV boundary, the shape of the corresponding PSF becomes wider and more asymmetric.

3.1.2. Reconstructed point sources. Figures 7(a) and 8(a) are central transverse and coronal sections of SSRB+FBP images while (b)–(d) are sections for FORE+FBP, FORE+OSEM and FORE+OSEM(DB) incorporating detector blurring PSFs (FORE+OSEM(DB)). Based on the results of figures 7 and 8, the SSRB was not explored further in this study. The results in figures 7 and 8 also indicate that incorporating detector blurring PSFs improves resolution recovery, while FBP and OSEM yield similar resolutions for this test object.

Radial profiles along the transverse axis in FORE reconstruction images (figures 7(b)–(d)) are shown in figure 9. The full-width-and-half-maximum (FWHM) values of those profiles are also displayed in table 1. Both results indicate that OSEM(DB) produces an improvement in resolution in terms of contrast and FWHM. Resolution is recovered more significantly at the FOV boundary.

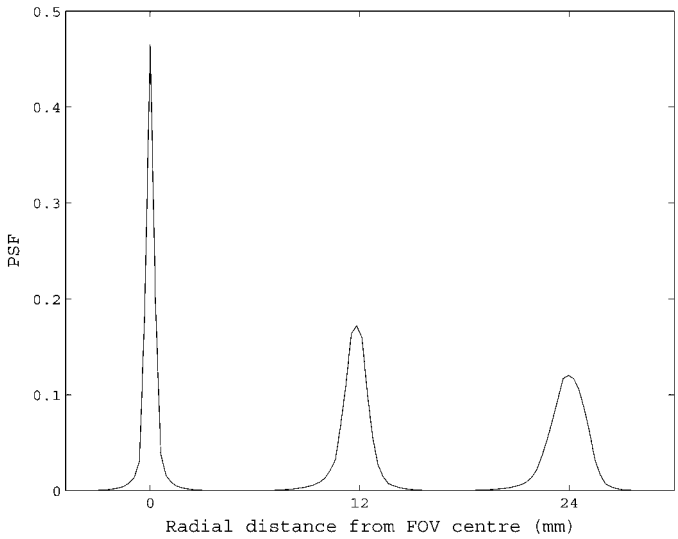

Figure 6. Transverse component of detector point-spread functions (PSF) at the centre, 12 and 24 mm off-centred position in projection domain.

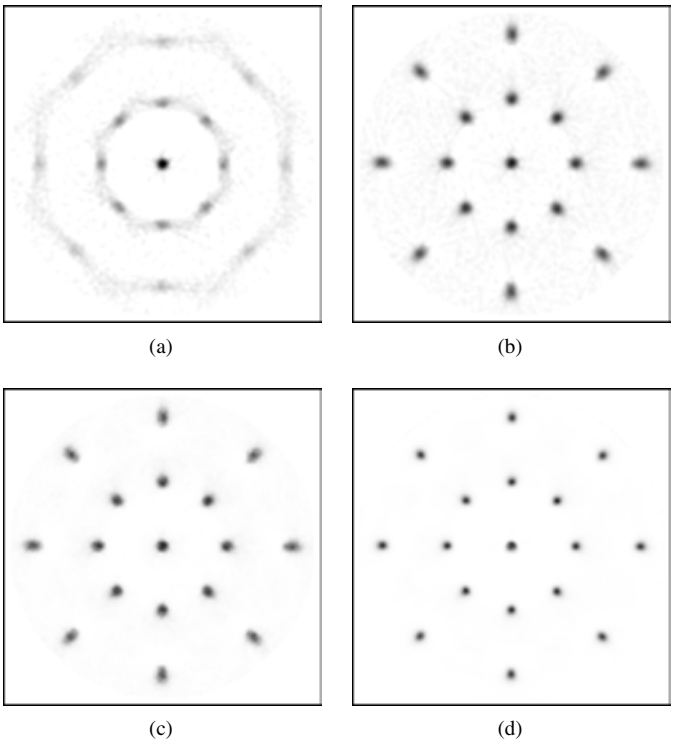

Figure 7. Transverse sections of reconstructed point source images with different methods. (a) SSRB+FBP, (b) FORE+FBP, (c) FORE+OSEM and (d) FORE+OSEM(DB).

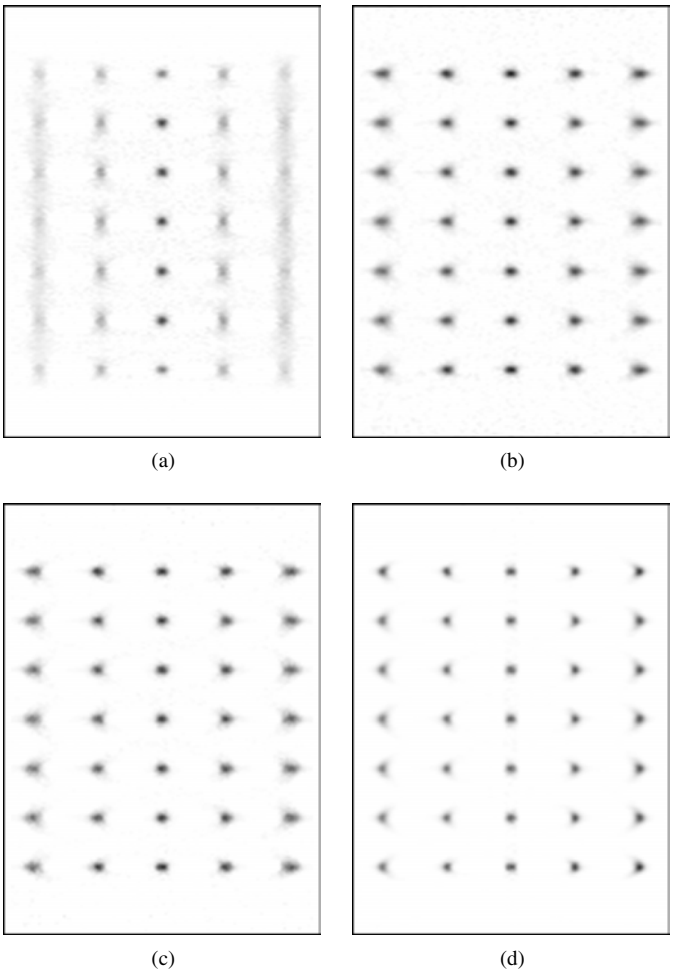

Figure 8. Coronal sections of reconstructed point source images shown in figure 7. (a) SSRB+FBP, (b) FORE+FBP, (c) FORE+OSEM and (d) FORE+OSEM(DB).

Table 1. FWHMs of reconstructed point sources in figure 7.

Reconstruction method	Centre (mm)	Twelve millimetre offset (mm)	Twenty-four millimetre offset (mm)
FBP	2.0	2.3	2.7
OSEM	1.9	2.1	2.6
OSEM(DB)	1.7	1.5	1.6

3.2. Measured data from the MiCES evaluation system

Figure 10(a) shows the sinograms of measured line source data without block alignment corrections for the (0, 14) mm radial offset line sources. The sinogram indicates significant distortion due to the misalignment of detector modules. Figure 10(b) shows the sinogram after block alignment correction, figure 10(c) shows the sinogram after sampling pattern

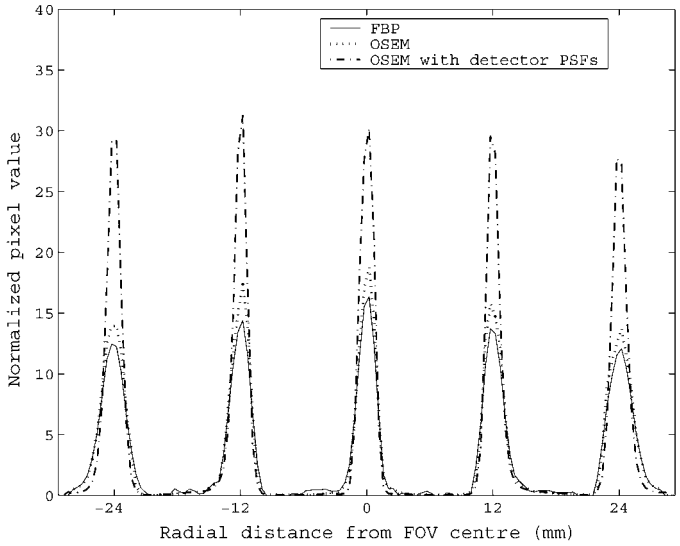

Figure 9. Radial profiles of reconstructed point sources in figures 7(b)–(d).

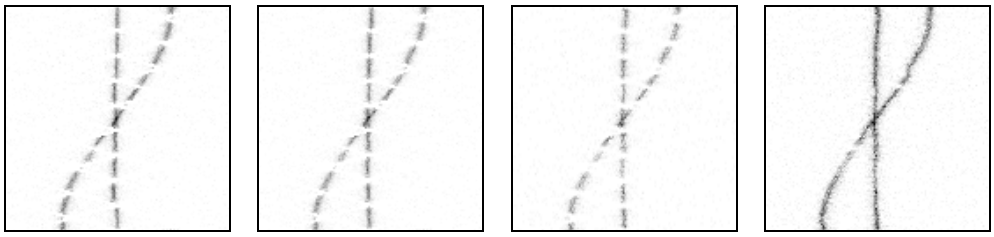

Figure 10. Intermediate sinograms corresponding to correction steps outlined in figure 5. (a) Before block alignment correction, (b) after block alignment correction, (c) after interference pattern normalization, (d) after adding second sinogram after 10° rotation.

normalization, and figure 10(d) shows the sinogram after gap compensation by adding rotated acquisitions. Some residual error in the block alignment is clearly visible.

3.2.1. Detector blurring point-spread functions. Figure 11(a) illustrates the change of σ_1 and σ_2 parameters estimated from fitted curves to transverse sinogram profiles (e.g. figure 10(d)) from off-centred positions (0, 14) to (14, 28) mm. A least-squares fit, which is represented by straight lines in figure 11(a), to the measured data indicates that the asymmetric property becomes more significant as the distance from the sinogram centre increases. The same trend was observed in the Lorentzian parameters (b_1, b_2) in equation (1). In addition, as shown in figure 11(b), the Gaussian weight w also varied with position. The increasing strength of the Gaussian term with transverse position implies narrower tails for the PSF at the transverse edges of the sinogram.

Figure 12 displays comparisons between sinogram PSFs acquired by measurements and those generated by parametrization at the centre and 12 mm radial positions. Comparisons at all positions showed good agreement between measured and fitted PSFs.

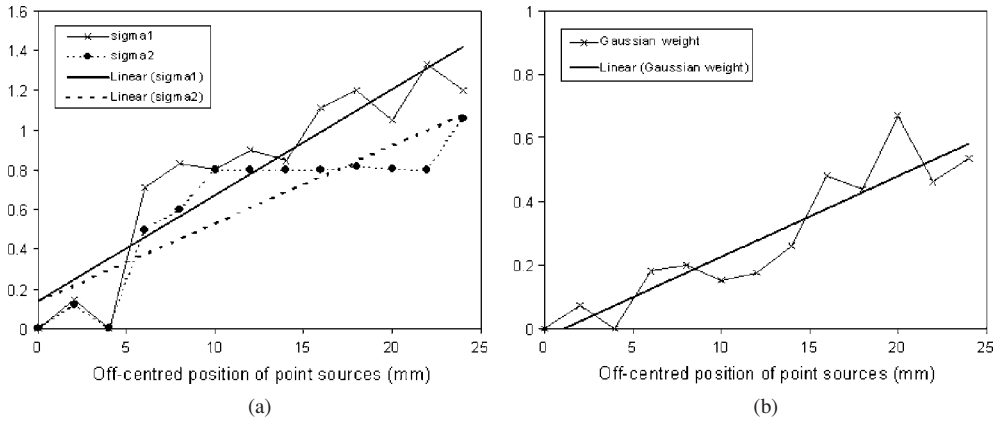

Figure 11. Estimated and least-squares linear fits to parameters in equation (1) as a function of the radial distance from the FOV centre. (a) Estimated and linear fits to Gaussian half-width parameters as a function of transverse position. (b) Estimated and linear fit to Gaussian weight term w in equation (1).

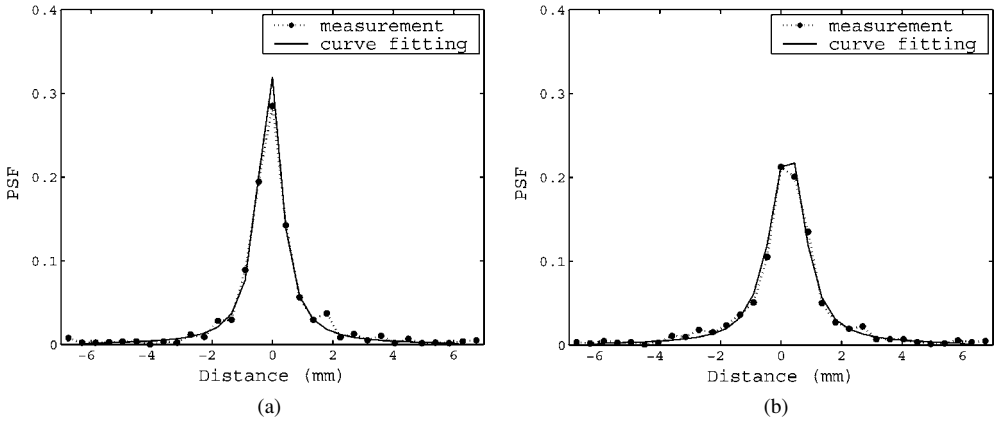

Figure 12. Experimentally measured detector PSFs and corresponding fitted-curves. (a) PSFs at the centre. (b) PSFs at 12 mm offset.

Figure 13 shows three PSFs generated by parametrization of off-centred positions 0, 12 and 24 mm. As implied in figure 11, the FWHM of the PSF becomes wider and more asymmetric as the source position moves away from the centre.

3.2.2. Image reconstruction of line source measurements. Figure 14 shows a sinogram and reconstructed images (transverse and coronal sections) of the combined line source listmode acquisitions. Images reconstructed by FORE+FBP (with a ramp filter), FORE+OSEM and FORE+OSEM(DB) are shown in figures 14(b)–(d). As also noted in the simulation studies, the proposed FORE+OSEM(DB) approach results in a more consistent resolution. In addition, the improvement is more conspicuous for line sources near the FOV boundary.

Radial profiles (figure 15) through the line source images also illustrate those improvements. FWHMs of the line sources at the centre were calculated from the reconstructed images by FORE+FBP, FORE+OSEM and FORE+OSEM(DB). The FWHM values of

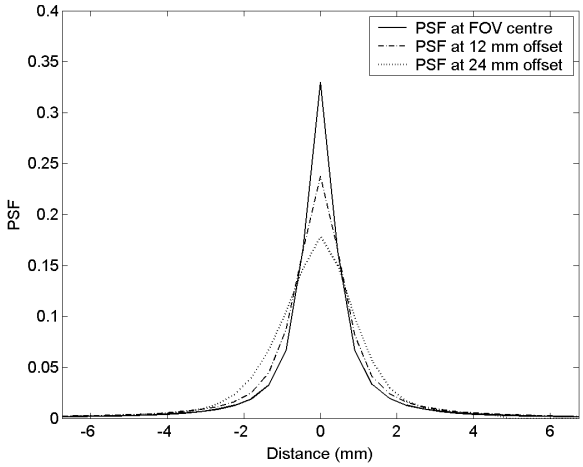

Figure 13. Experimental detector point spread-functions at the FOV centre, 12 and 24 mm off-centred position in sinogram.

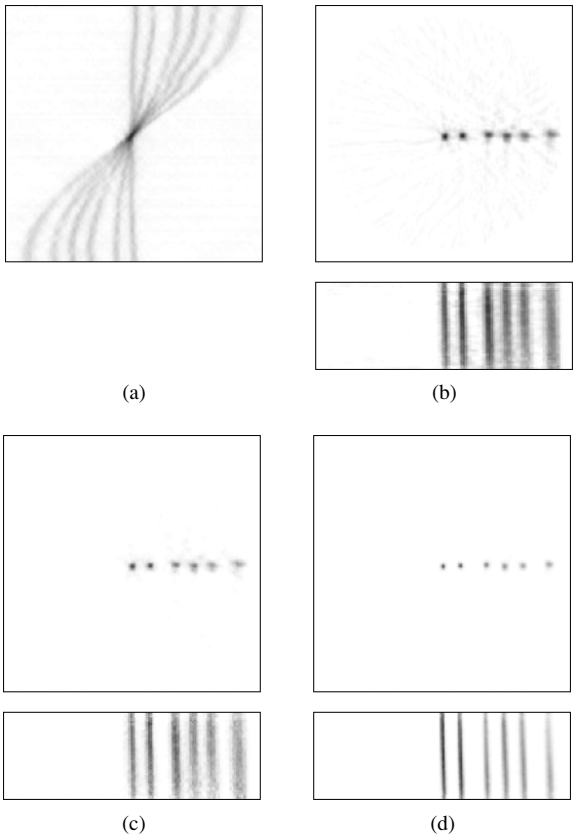

Figure 14. (a) Sinogram and images of line sources rebinned with the FORE and reconstructed with different method: (b) FORE+FBP, (c) FORE+OSEM and (d) FORE+OSEM(DB).

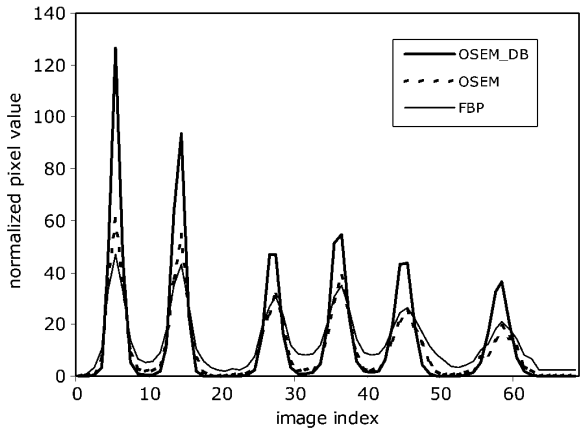

Figure 15. Radial profiles through reconstructed point sources shown in figures 15(b)–(d).

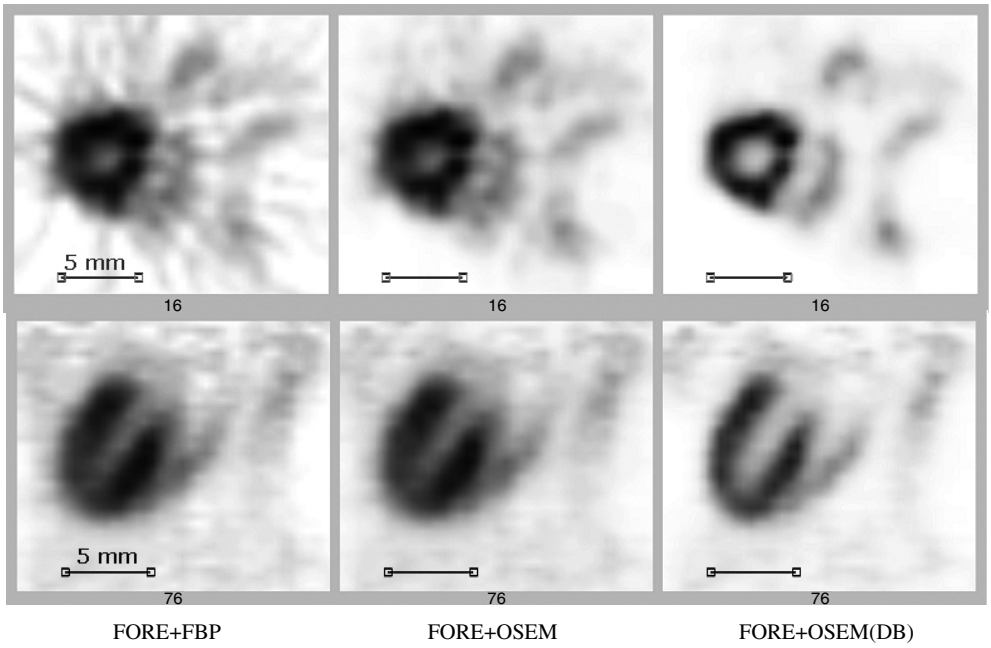

Figure 16. Transverse and coronal mouse heart images from three different reconstruction methods: FORE+FBP (left) FORE+OSEM (middle) and FORE+OSEM(DB) (right).

reconstructed point sources at the centre were 1.3, 1.1 and 0.7 mm for the three methods, implying a potential for resolution improvement by the proposed method.

3.2.3. Reconstruction of mouse cardiac images. Figure 16 shows transverse and coronal sections of mouse heart images reconstructed with the three different reconstruction techniques.

The images on the left were reconstructed with FORE+FBP. The middle images used FORE+OSEM. As shown in the figure, OSEM suppresses low-level noise as expected. The

images on the right are results obtained by FORE+OSEM(DB) with incorporated detector blurring. The FORE+OSEM(DB) images are sharper than the others, which implies that the inclusion of non-stationary detector blurring PSFs within the system matrix can significantly improve image resolution.

4. Discussion

The proposed method (FORE+OSEM(DB)) is modelled on fully 3D image reconstruction used in clinical PET scanners, which is based on FORE rebinning followed by 2D OSEM iterative image reconstruction. In addition, we also used a factorized system model that incorporated resolution-sensitive physical effects in PET, in particular non-stationary detector blurring. This approach makes approximations that will reduce some measures of image quality as compared to those produced by a Bayesian model of the complete acquisition process (Qi *et al* 1998, Leahy and Qi 2000). In particular the effects of positron range and detector efficiencies are not modelled, as well as blurring in the axial direction. Including these effects in the modelling of the system could improve the tradeoffs between noise and contrast or resolution. The benefit, however, in concentrating on the most significant effects is a simplified model and decreased image reconstruction time. The relative merits of these two approaches, which will be the subject of further study, is a complex issue that depends on several factors including scanner design, choice of radioisotope, imaging task and scanner throughput.

The simulation studies were used to test the basic efficacy of the approach where we have perfect knowledge of the detector blurring. For the measured data from the evaluation system, we did not attempt to simulate the detector PSF, but rather used an estimate of the transverse PSF blurring derived from line source measurements. For the full four-ring MiCES scanner, our plan is to also measure the detector blurring PSF directly.

Since the imaging study so far has been based on ^{18}F, the detector blurring effect is a more dominant effect on resolution recovery than positron range (Lee *et al* 2004). Therefore positron range is not included in the current system model. For higher energy positron emitters, however, the range effect is important, albeit potentially difficult to model in inhomogeneous media.

For both the simulated and measured data, the PSF was two dimensional on the detector surface for each end of the line of response. In the image reconstruction, however, only the transverse effect was modelled.

5. Conclusions

Reconstructions using the proposed method were presented from point source simulations and measured data from the QuickPET II system that were compared with images reconstructed by traditional methods in clinical imaging (FORE+FBP and FORE+OSEM). The results indicate that the proposed FORE+OSEM(DB) approach, which incorporated detector blurring PSFs, improved image resolution in terms of both contrast and FWHM without undue increases in noise. This apparent improvement in performance, however, remains to be demonstrated with estimation of true noise behaviour across multiple realizations, and is currently under study.

Acknowledgments

This work was supported by National Institutes of Health under grants CA-74135, CA-86892 and EB0217. We acknowledge helpful discussions with Dr Richard Leahy of USC and the assistance of Barbara Lewellen with the mouse experiments.

References

Chatziioannou A 2002 Molecular imaging of small animals with dedicated PET tomographs *Eur. J. Nucl. Med.* **29** 98–114

Chatziioannou A F, Cherry S R, Shao Y, Silverman R W, Meadors K, Farquhar T H, Pedarsani M and Phelps M E 1999 Performance evaluation of microPET: a high-resolution lutetium oxyorthosilicate PET scanner for animal imaging *J. Nucl. Med.* **40** 1164–75

Cherry S R 2004 *In vivo* molecular and genomic imaging: new challenges for imaging physics *Phys. Med. Biol.* **49** R13–48

Comtat C, Kinahan P E, Defrise M, Michel C and Townsend D W 1998 Fast reconstruction of 3D PET data with accurate statistical modeling *IEEE Trans. Nucl. Sci.* **45** 1083–9

Daube-Witherspoon M E and Muehllehner G 1987 Treatment of axial data in three-dimensional PET *J. Nucl. Med.* **28** 1717–24

Defrise M, Kinahan P E, Townsend D W, Michel C, Sibomana M and Newport D F 1997 Exact and Approximate Rebinning Algorithms for 3-D PET Data *IEEE Trans. Med. Imaging* **16** 145–58

Defrise M and Kinahan P 1998 Data acquisition and image reconstruction for 3D PET *The Theory and Practice of 3D PET* ed D W Townsend and B Bendriem (Dordrecht: Kluwer Academic) pp 11–54

Fessler J A 2001 Aspire 3.0 User's Guide: A Sparse Iterative Reconstruction Library Technical Report No. 293 Communications & Signal Processing Laboratory, University of Michigan

Fessler J A 2002 Users Guide for Aspire 3D Image Reconstruction Software Technical Report No. 310 Communications & Signal Processing Laboratory, University of Michigan

Fessler J A 2003 Dynamic Libraries for ASPIRE Penalty Functions and System Models Communications & Signal Processing Laboratory, University of Michigan

Frese T, Rouze N C, Bouman C A, Sauer K and Hutchins G D 2003 Quantitative comparison of FBP, EM, and Bayesian reconstruction algorithms for the IndyPET scanner *IEEE Trans. Med. Imaging* **22** 258–76

Hudson H and Larkin R 1994 Accelerated image reconstruction using ordered subsets of projection data *IEEE Trans. Med. Imaging* **13** 601–9

Johnson C A, Seidel J, Carson R E, Gandler W R, Sofer A, Green M V and Daube-Witherspoon M E 1997 Evaluation of 3D reconstruction algorithms for a small animal PET scanner *IEEE Trans. Nucl. Sci.* **44** 1303–8

Leahy R M and Qi J 2000 Statistical approaches in quantitative positron emission tomography *Stat. Comp.* **10** 147–65

Lee K, Kinahan P E, Miyaoka R S, Kim J and Lewellen T K 2004 Impact of system design parameters on image figures of merit for a mouse PET scanner *IEEE Trans. Nucl. Sci.* **51** 27–33

Liang Z 1994 Detector response restoration in image reconstruction of high resolution positron emission tomography *IEEE Trans. Med. Imaging* **13** 314–21

Liu X, Comtat C, Michel C, Kinahan P E, Defrise M and Townsend D W 2001 Comparison of 3-D reconstruction with 3D-OSEM and with FORE+OSEM for PET *IEEE Trans. Med. Imaging* **20** 804–14

Matej S, Karp J S, Lewitt R M and Becher A J 1998 Performance of the Fourier rebinning algorithm for PET with large acceptance angles *Phys. Med. Biol.* **43** 787–95

Miyaoka R S, Janes M L, Park B K, Lee K, Kinahan P E and Lewellen T K 2003 Toward the development of a micro crystal element scanner (MiCES): QuickPET II *IEEE Nuclear Science Symp. and Medical Imaging Conf. (Portland, OR)*

Miyaoka R S, Kohlmyer S G and Lewellen T K 2001 Performance characteristics of micro crystal element (MiCE) detectors *IEEE Trans. Nucl. Sci.* **48** 1403–7

Mumcuoglu E U, Leahy R M, Cherry S R and Hoffman E 1996 Accurate geometric and physical response modeling for statistical image reconstruction in high resolution PET *IEEE Nuclear Science Symp. and Medical Imaging Conf.* vol 3 pp 1569–73

Qi J, Leahy R M, Chatziioannou A and Farquhar T H 1998 High-resolution 3D Bayesian image reconstruction using the microPET small-animal scanner *Phys. Med. Biol.* **43** 1001–13

Reader A J, Ally S, Bakatselos F, Manavaki R, Walledge R J, Jeavons A P, Julyan P J, Sha Z, Hastings D L and Zweit J 2002 One-pass list-mode EM algorithm for high-resolution 3-D PET image reconstruction into large arrays *IEEE Trans. Nucl. Sci.* **49** 693–9

Selivanov V V, Picard Y, Cadorette J, Rodrigue S and Lecomte R 2000 Detector response models for statistical iterative image reconstruction in high resolution PET *IEEE Trans. Nucl. Sci.* **47** 1168–75